

PAPER

Waveform analysis of a large-area superconducting nanowire single photon detector





To cite this article: Claire E Marvinney *et al* 2021 *Supercond. Sci. Technol.* **34** 035020

View the [article online](#) for updates and enhancements.

You may also like

- [Waveguide integrated superconducting nanowire single-photon detectors for integrated photonics](#)
Vidur Raj, Adan Azem, Max Patterson et al.
- [Superconducting nanowire single-photon detectors: physics and applications](#)
Chandra M Natarajan, Michael G Tanner and Robert H Hadfield
- [Heat transfer in superconducting nanowire single-photon detectors: mechanism and modulation](#)
Wenlei Yin, Hao Wang, Xiaohan Wang et al.

Waveform analysis of a large-area superconducting nanowire single photon detector

Claire E Marvinneyce¹ , Brian E Lerner¹ , Alexander A Puretzky¹ , Aaron J Miller² and Benjamin J Lawrie¹ 

¹ Oak Ridge National Laboratory, 1 Bethel Valley Rd, Oak Ridge, TN 37831, United States of America

² Quantum Opus, LLC, 22241 Roethel Dr Ste A, Novi, MI 48375, United States of America

E-mail: marvinneyce@ornl.gov and lawrie@ornl.gov

Received 12 November 2020, revised 13 November 2020

Accepted for publication 7 December 2020

Published 2 February 2021



Abstract

Superconducting nanowire single photon detectors (SNSPDs) are typically used as single-mode-fiber-coupled single-pixel detectors, but large area detectors are increasingly critical for applications ranging from microscopy to free-space quantum communications. However, the long meander-line length of such large-area SNSPDs results in a proportionately large kinetic inductance that affects the waveform generated by the device. Here, we explore changes in the rising edge of the readout pulse for a single-pixel large-area SNSPD as a function of the optical spot size on the detector and compare to the rising edge of the dark-count waveform. We observe a bimodal distribution of bright-count rise times and show that the probability of a slow rise time increases in the limit of large spot sizes, indicative of a position sensitive response. Additionally, in the limit of low bias currents, the dark-count readout pulse is most similar to the large spot-size bright-count readout pulse, which suggests that dark counts arise from locations spanning the device. These results are consistent with a simple model of traveling microwave modes excited by single photons incident at varying positions along the length of the nanowire.

Keywords: superconducting nanowire single photon detectors, SNSPDs, large area single photon detectors, superconducting devices

(Some figures may appear in colour only in the online journal)

Superconducting nanowire single photon detectors (SNSPDs) have³ become increasingly relevant to quantum networking [1–5] and quantum sensing [6, 7] because they offer

high-speed, high-quantum-efficiency, and low dark-count-rate single photon detection [8, 9]. Readout-pulse analysis has been used to provide spatially resolved detection [10] and few-photon number resolution [11–13] in single-channel SNSPDs. In parallel with these device developments, a growing demand has emerged for large-area SNSPDs capable of providing high collection efficiency for applications ranging from microscopy to satellite communications [10, 14–16]. However, the signals produced by large-area SNSPDs are not always directly comparable to those produced by single-mode SNSPDs. A fundamental understanding of the waveforms produced by large-area SNSPDs is therefore essential to future progress in these fields.

³ This manuscript has been authored by UT-Battelle, LLC under Contract No. DE-AC05-00OR22725 with the U.S. Department of Energy. The United States Government retains and the publisher, by accepting the article for publication, acknowledges that the United States Government retains a non-exclusive, paid-up, irrevocable, world-wide license to publish or reproduce the published form of this manuscript, or allow others to do so, for United States Government purposes. The Department of Energy will provide public access to these results of federally sponsored research in accordance with the DOE Public Access Plan (<http://energy.gov/downloads/doe-public-access-plan>).

In large-area SNSPDs, the kinetic inductance (proportional to the nanowire length) can be over an order of magnitude larger than that of a single-mode SNSPD [17], leading to poor impedance matching using traditional electronics, which can in turn lead to decreased maximal count rates [18] and increased detector reset times [19]. The increased nanowire length also increases the signal propagation delay. For a 2 mm long nanowire, the propagation delay can be on the order of the hot-spot formation time of 200 ps [20, 21]. Together, the increased kinetic inductance and propagation delay of large-area SNSPDs must be considered in order to provide a reasonable understanding of the SNSPD waveform.

Here, we use high-speed signal analysis to characterize the waveforms generated by large-active-area ($30 \times 30 \mu\text{m}$) SNSPDs optimized for visible photon detection and integrated with low-noise cryogenic and room temperature amplifiers. The large-active-area SNSPDs used in this experiment are a custom design by Quantum Opus, LLC that utilize a proprietary amorphous superconducting material for visible photon detection. These devices have a 95 nm nanowire width, 50.5% fill fraction, and approximately 7 nm thickness. By contrast, standard telecom devices (described in the appendix) have a $5 \times 5 \mu\text{m}$ active-area with a 50% fill fraction of 60 nm width, 6 nm thick nanowires. The telecom devices have a quantum efficiency (QE) of $>80\%$ at 1550 nm, dark count rates of $<100 \text{ cts s}^{-1}$, and jitter of $<50 \text{ ps}$. The $30 \times 30 \mu\text{m}$ SNSPDs have a comparably high QE from 60% to 80% for wavelengths ranging from 400 to 1000 nm, improved dark count rates of $<10 \text{ cts s}^{-1}$, and electronic jitter comparable to the telecom devices, though there is a nominal increase in the jitter associated with the longer length of the nanowire.

A general schematic of the experiment is shown in figure 1. The rise time of the readout pulse is characterized as a function of photon number per pulse (μ), bias current, and spot size on the detector. The rise-time of an SNSPD corresponds to the transition from the superconducting to normal state in a localized hot-spot. SNSPDs are not generally used for $\mu > 1$ because they do not typically provide photon number resolution. Similarly, they are typically operated at a bias current that produces <100 dark counts per second. However, characterizing the changes in readout waveforms for large μ and large bias currents helps to generate a basic understanding of the waveforms acquired for typical single-photon counting operating parameters. Additionally, varying the spot size on the detector allows us to explore spatial variations in the readout waveforms that do not appear in smaller single-mode detectors in order to understand the changes in device behavior in large area, large kinetic-inductance devices.

The detector studied in the main text was cooled to 2.25 K and held at a constant bias current of $6.50 \mu\text{A}$ (where the detector has a dark-count rate of $2 - 4 \text{ cts s}^{-1}$ and the detector efficiency has plateaued as shown in appendix A.1) for all bright-count measurements. The attenuated second harmonic of a Ti:sapphire oscillator with a 2 ps pulse duration, 400 nm wavelength, and 1 MHz rep rate was used as the bright count light source, and the mean photon number per pulse was varied from $\mu = 0.01$ to $\mu = 700$ with neutral density filters. The light was fiber coupled from the laser using a variety

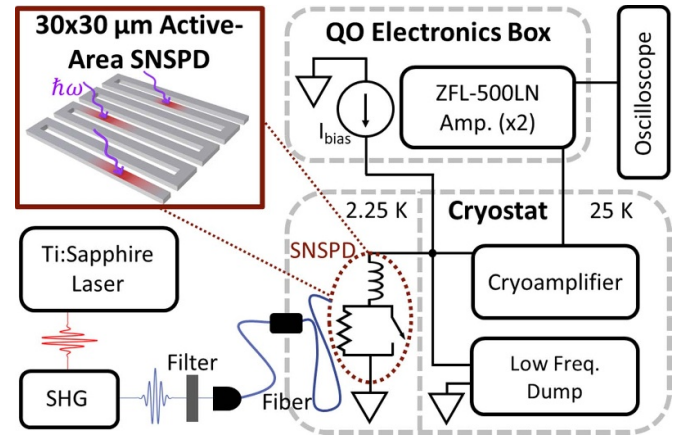


Figure 1. Schematic of the experiment used for collecting rise-time histograms and waveforms of the SNSPD readout pulse. Inset of the superconducting nanowire meander line geometry, not to scale, demonstrating the basic process of photon-induced hotspot formation.

of fiber patch cables in order to change the spot size of the light on the SNSPD, as shown in the inset of figure 2(b). Readout pulse signals were collected on a 33 GHz oscilloscope. The resulting waveforms and histograms of the waveform 20%–80% rise time are presented here. Dark-count waveforms were acquired with fibers removed and all external light to the devices blocked for bias currents of $6.50 - 9.68 \mu\text{A}$, corresponding to dark-count rates spanning six orders of magnitude. The bias currents selected for dark count waveform characterization are marked on the counts versus bias plot in appendix A.1.

As the optical spot size was varied, no notable changes were observed in the signal amplitude, so we focus here on the rise-time distribution. For small mean photon number, a bimodal distribution exists in the histogram of rise times as shown in figure 2(a), with the centroids of the two modes at 0.57 and 1.50 ns and a $2 \times$ greater probability of measuring a rise time that falls in the faster mode. Larger spot sizes substantially increase the probability of a slower rise time for a constant photon count rate. When illuminated with a $33 \mu\text{m}$ donut mode, the rise time is six times more likely to fall in the slower mode than when illuminated with a $7 \mu\text{m}$ spot size. However, for average photon number much larger than 1, the slow mode of the bimodal distribution disappears, and the centroid of the faster mode moves to 0.41 ns for all beam spot sizes, as shown in figure 2(b).

The relationship between rise time and μ becomes more apparent in the histogram of rise times for constant $7 \mu\text{m}$ spot size and variable μ shown in figure 2(c). Only the fast component of the readout waveform is present for this relatively small spot size, and for $\mu < 10$, the rise-time distribution is independent of μ . As μ continues to increase to 1270, the centroid of the rise-time distribution decreases from 0.57 to 0.40 ns with a corresponding reduction in the full-width half-maximum (FWHM) of the distribution from 0.18 to 0.06 ns.

Figure 2(d) illustrates the intrinsic dark-count rise-time histograms for variable bias current. For bias currents of 6.50 and $7.48 \mu\text{A}$ (corresponding to dark count rates of 2

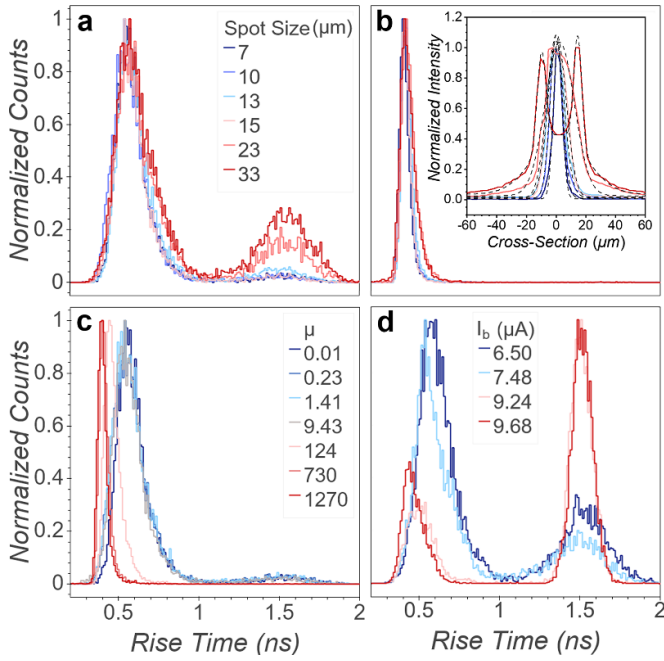


Figure 2. SNSPD 20%–80% rise-time histograms with mean photon number per pulse $\mu = 0.01$ (a) and $\mu = 700$ (b) for varying spot size on the detector (legend in (a)). Cross-sections of the beam profiles at the tip of each fiber are shown in the inset of (b) with corresponding fits. The same multimode fiber was used to generate 23 and 33 μm spots, with modified fiber incoupling resulting in a shift from a quasi-Gaussian mode to a donut mode. (c) Bright-count rise-time histograms for variable μ and a 7 μm spot size. (d) Intrinsic dark-count rise-time histograms for variable bias current.

and 100 cts s^{-1} respectively), the bimodal distribution with centroids of 0.59 and 1.53 ns and a ratio between the faster and slower modes of 2 to 1 is consistent with the bright-count rise-time histograms for small μ and large spot size in figure 2(a). However, as the bias current increases to 9.24 and 9.68 μA (corresponding to dark count rates of 100 000 and 3 000 000 cts s^{-1} , respectively), the device moves into an electrothermal oscillation regime in which a hotspot periodically forms and quenches with frequency determined by the device inductance and load impedance [21–24]. In this high bias-current limit, the relative probability of the slow mode climbs to $2\times$ that of the fast mode, and the faster of the dark-count rise-time peaks shifts from 0.59 to 0.46 ns, consistent with the change in the fast bright-count rise-time distribution with increasing μ shown in figure 2(c), though the FWHM of the faster peak does not decrease as substantially with bias current.

While there are correlations evident between the histograms plotted in figure 2, it is difficult to fully understand these correlations without examining the SNSPD readout waveforms directly. Figures 3(a) and (b) depict 100 waveforms in a digital persistence mode acquired for 7 and 23 μm spot sizes and $\mu = 0.01$. Two notable characteristics of the waveforms are (1) the sinusoidal modulation of the signal (with frequency components at 0.4, 0.5, and 0.6 GHz), and (2) the overshoot past 0 V at 8.45 ns after the initial pulse.

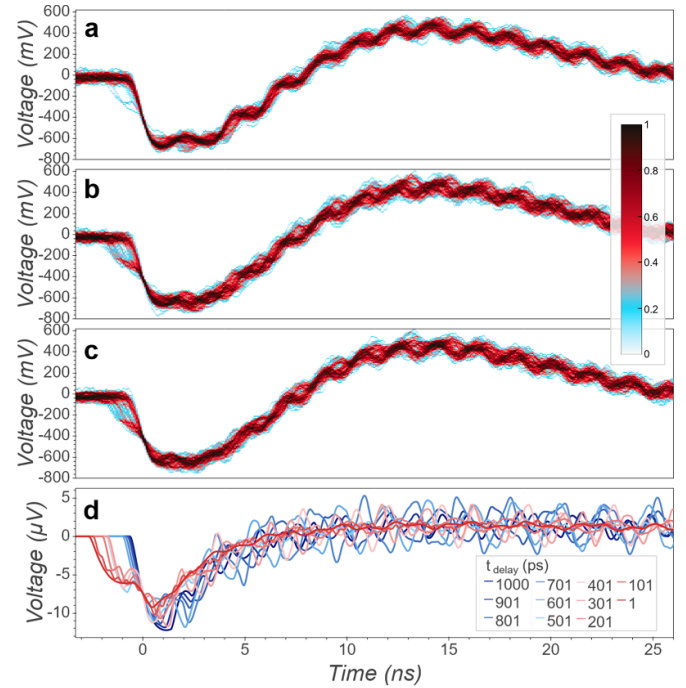


Figure 3. 100 waveforms of the bright count data collected in digital persistence mode at $\mu = 0.01$ for spot sizes of (a) 7 μm and (b) 23 μm . (c) 100 waveforms of dark count data for the typical operating bias current of 6.50 μA . Waveforms are inverted by the cryoamplifier. (d) Simulated waveforms for photons incident at 11 positions on the nanowire defined by the microwave propagation time along the nanowire (shorter propagation times correspond to positions closer to the device readout).

A LTspice model [25] was created to predict whether variation in the photon arrival position on the SNSPD could lead to characteristics (1) and (2), using a lumped element depiction of the hotspot formation [21] as shown in figure 1, where the most notable characteristic from the experimental waveform data used to create the simulation is characteristic (1), the sinusoidal modulation frequency, as described below. The simulated position-dependent waveforms are shown in figure 3(d), with a magnified view of the rising edge of the waveforms included in appendix A.2. The simulation parameters include the kinetic inductance of 10 μH of the device, which is extrapolated from experimental measurements of smaller telecom devices. We assume the large-area devices studied here have an approximately 16-fold increase in their kinetic inductance due to their increased length and use of a single-readout instead of dual-readout configuration. A square resistance of $575 \Omega \text{ sq}^{-1}$ is calculated and consistent with the smaller devices. In these simulations, however, unlike in the typical lumped element model of the entire SNSPD device, the position of a photon incident on the nanowire is simulated by varying the microwave propagation time after initial photon absorption, with shorter time delays closer to the readout circuit. The sinusoidal oscillations are a characteristic of pulse echos of the propagating signal within the length of the meander line, and thus the oscillation frequency can be used to approximate the phase velocity of the signal as $v_p = \lambda f$ [26], where λ is double the total length of the meander line.

The microwave propagation delay time is determined to be 1000 ps based on the 4.79 mm total nanowire length and the average pulse echo frequency of 0.5 GHz. This indicates that $v_p = 0.016c_0$, consistent with previous calculations [20]. The pulse is simulated using the $575 \Omega \text{ sq}^{-1}$ square resistance with a 3.0 ns on-time voltage switch that results from the slower hotspot formation due to the large kinetic inductance relative to the hotspot resistance. The characteristic impedance of the nanowire meander line is $Z = \sqrt{L/C} = 10 \text{ k}\Omega$, where L is the $10 \mu\text{H}$ inductance and C is calculated from the phase velocity of the nanowire $v_p = 1/\sqrt{L_n C_n}$ where L_n and C_n are the inductance and capacitance per unit length, respectively [20]. This leads to $C = 100 \text{ fF}$. Given these parameters, the simulated waveforms qualitatively match the experimental waveforms in shape with sinusoidal oscillations ranging from 0.36–0.46 GHz and 0.63–1.10 GHz, consistent with the observed experimental frequencies. The simulated waveform in figure 3(d) is a representation of the raw SNSPD pulse before amplification. In practice, the SNSPDs were connected to a high-pass filter before going through the amplification circuit that has a simulated 3 dB high-pass knee at 33 MHz and a 3 dB low-pass knee at 1 GHz. The filter and poor impedance matching of the amplifiers with the meander line lead to the overshoot of 0 V at an average of $7.12 \pm 1.48 \text{ ns}$ in the simulation, also in rough agreement with experiment.

The frequency, amplitude, and shape of the rising edge of the oscillations in the simulated SNSPD readout pulse vary as the incident photon position is varied from the grounded end (1000 ps) to the coax-connected end (1 ps) of the nanowire delay line as shown in figure 3(d). At the grounded end of the nanowire, a 20%–80% rise time of 0.67 ns is observed; toward the middle of the nanowire, the rise time begins to slow as a ripple forms in the rising edge; and toward the coax-connected end of the of the nanowire, all waveforms have a ripple in the rising edge and the oscillations decrease in amplitude, leading to slower rise times of 2.29 ns. These modeled variations in the SNSPD rise time are qualitatively consistent with the measured bimodal rise-time histograms for large spot sizes that illuminate the entirety of the nanowire meander line. In experiment, this suggests that for the largest spot sizes, photons incident near the coax-connected end of the detector yield slower rise times, while faster rise times are measured for photons incident toward the grounded end of the nanowire. For the smaller spot sizes in figure 2(a), the slowest rise times that correspond to the coax-connected side of the device are negligible as the light only illuminates the center region of the device. The simulation does not match perfectly, as photons arriving in the center of the device can elicit either a fast or a slow rising edge to the readout waveform, but the simulation does confirm that the rising edge speed of the waveform depends on position, with photons incident near the center and the grounded end of the nanowire delay line inducing the fastest rise-time.

These experimental measurements were repeated with a second large active-area SNSPD, and the waveforms in appendix A.3 also qualitatively match both the device studied here and the simulated, position-dependent waveforms,

most notably with a ripple in the rising edge of the waveform appearing at larger beam spot sizes. In addition, the geometry of the device shown in appendix A.3 is for a slightly shorter, 3.93 mm length meander line (as described in appendix A.3), and the resulting pulse-echo sinusoidal oscillations in the waveforms are faster, with characteristic frequencies of 0.4 and 0.7 GHz. Both the decrease in length corresponding to an increase in oscillation frequency and the ripple occurring in the rising edge for larger illumination spot sizes are consistent with our previous analysis.

The meander line position sensitivity evident in the experimental and modeled data can thus be understood as a result of the propagation delay in the long meander line and the corresponding pulse echo that generates the sinusoidal modulation of the readout pulse due to the impedance mismatched meander line acting as a shorted microwave line. At the grounded end of the nanowire, the microwave signal can only propagate in a single direction, but as the detection event approaches the coax connected end of the nanowire, the signal can also propagate backwards, leading to pulse echo interference with the forward propagating signal. This effect results in the bimodal rise-time histogram for the small μ , large area pulses seen in figure 2(a). Similarly, the bimodal dark-count rise-time histogram for small bias currents in figure 2(d) can be understood as a result of roughly uniformly distributed dark count events across the length of the meander line. The dark-count waveforms at low bias currents, shown in figure 3(c), appeared nearly identical to the large spot-size bright count waveforms, as do the dark-count waveforms for the second large-active area device in appendix A.3. Thus, under typical operating conditions, dark counts are not triggered from a single defect in the nanowire meander line, but instead from a random selection from a large distribution of defects across the entire span of the detector, consistent with a large spot size photon source and other recent experiments [10].

Additionally, dark count waveforms were collected from a $5 \times 5 \mu\text{m}$ active area telecom SNSPD from Quantum Opus, LLC, as shown in appendix A.3. While this third device does have a pulse echo oscillation of about 2.2 GHz, consistent with its much shorter length and smaller inductance, there is no variation between any of the waveforms, suggesting that small-area devices do not exhibit a position-dependent waveform within the bandwidth of commercial readout electronics.

While the LTspice simulation describes the position dependence of the signal readout pulse under typical single-photon counting operating conditions, it does not yet describe the limiting cases of high bias currents when the device is exhibiting electrothermal oscillations or of high μ where locations across the entire device are being driven normal. In the high bias-current electrothermal oscillation regime, both modes of the bimodal rise time distribution have smaller FWHMs (bias currents $> 7.48 \mu\text{A}$ in figure 2(d)) than under typical operating conditions and the waveforms in figure 4(a) have a uniform appearance. The spatial dependence observed at lower bias currents disappears as the bias current exceeds the critical current, potentially indicating that only the weakest single or few locations are triggering in this regime. At

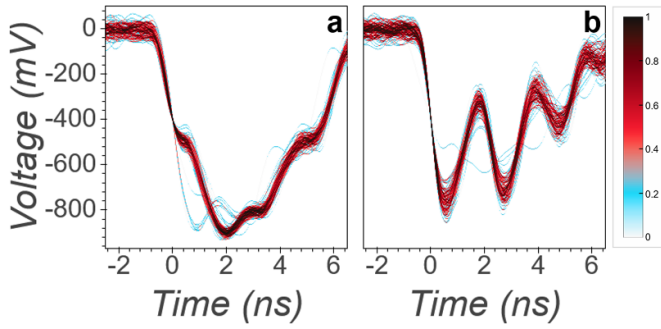


Figure 4. 100 waveforms collected in digital persistence mode under dark conditions at the highest bias current of $9.68 \mu\text{A}$ where electrothermal fluctuations lead to 3 Mcps (a) and under bright conditions with a high $\mu = 700$, typical bias current of $6.50 \mu\text{A}$, and a $33 \mu\text{m}$ spot size sending photons to the entire detector (b) (waveforms are inverted by the cryoamplifier).

high photon numbers and typical bias currents of $6.50 \mu\text{A}$, the device similarly operates outside the typical single-photon counting regime; here the large number of simultaneous photons provide enough energy to drive large sections of the device normal at once. This increases the total hotspot resistance in the nanowire, and again eliminates the spatial dependence to the waveform as seen in figure 4(b). LTspice simulations confirm that increasing the hotspot resistance from 575Ω to $40 \text{ k}\Omega$ increases the amplitude of the position-dependent sinusoidal oscillations from roughly a quarter of the voltage maximum to roughly half of the voltage maximum, consistent with the experimental waveforms observed in figures 3(a) and (b) and figure 4(b), respectively. Simulations incorporating an electro-thermal model of the hotspot formation [23] may better predict the high bias and high μ cases of operation where there is a combination of an increased number of hotspots, larger hotspot areas, and potential variations in the switching dynamics that cannot be captured with a simple switch.

To date, most research involving SNSPDs has relied on single mode fiber-coupling or on complex multi-channel devices, and thus the spatial sensitivity and dependence of the SNSPD waveform within a single meander line has remained poorly explored. As the demand for large-area SNSPDs increases for applications ranging from microscopy to free-space quantum communications, an exploration of spatial sensitivity of the read-out pulse, like that presented here, is increasingly critical to improving and optimizing device design. The experiments presented here show that large-area SNSPDs have a position sensitive readout signal that varies between the coax-connected end and grounded end of the detector due to pulse echos of the microwave signal. Additionally, this position sensitivity is evident not only in the bright count data, but also the dark count data, indicating that dark counts observed during typical single-photon counting operation arise from defect positions spanning the entire detector rather than from a small number of defect sites. Improvements in the position sensitivity reported here could lead to a complete position dependence of the signal, which could lead to methods for filtering out dark counts in post processing or for

spectrally resolved single photon detection for SNSPDs incorporating diffraction gratings.

Acknowledgments

This research was sponsored by the U.S. Department of Energy, Office of Science, Basic Energy Sciences, Materials Sciences and Engineering Division. Student (BEL) and postdoctoral (CEM) research support were provided by the Intelligence Community Postdoctoral Research Fellowship Program at the Oak Ridge National Laboratory, administered by Oak Ridge Institute for Science and Education through an interagency agreement between the U.S. Department of Energy and the Office of the Director of National Intelligence and by the DOE Science Undergraduate Laboratory Internships (SULI) program. SNSPD measurements with pulsed laser sources were conducted at the Center for Nanophase Materials Sciences, which is a DOE Office of Science User Facility. The authors thank Matthew A Feldman for support with microwave electronics.

The data that support the findings of this study are available from the corresponding author upon reasonable request.

Appendix A

A.1. Bright counts as a function of bias current

Bright counts and dark counts were measured as a function of bias current for the $30 \times 30 \mu\text{m}$ active-area SNSPD studied in the main text. The bright counts were measured with a spectrally filtered white light source ($\lambda = 600, 800, 1000 \text{ nm}$) and dark counts were measured with the system capped. The results are shown in figure 5. The four bias currents used for all the histogram and waveform measurements are indicated with dashed lines, with all the bright count measurements taken on the plateau of the device at $6.50 \mu\text{A}$ before the dark counts begin to increase. The experimental histogram and waveform dark count measurements were taken at all four indicated bias currents.

A.2. Additional simulation results

Figure 6 depicts the experimental and simulated waveforms from the main text, but over a shorter timescale centered on the rising edge of the waveform. The qualitative similarities such as the ripple in the rising edge of the waveform are clearly evident in both the experimental waveforms and the simulated waveforms.

A.3. Measurements of additional devices

Waveforms were measured for two additional Quantum Opus, LLC devices and are shown in figure 7. The second device is a $30 \times 30 \mu\text{m}$ active-area visible wavelength SNSPD, similar to the one studied in the main text. This second large-active-area SNSPD has a 115 nm nanowire width instead of a 95 nm nanowire width, with a fill fraction of 50.2%, and

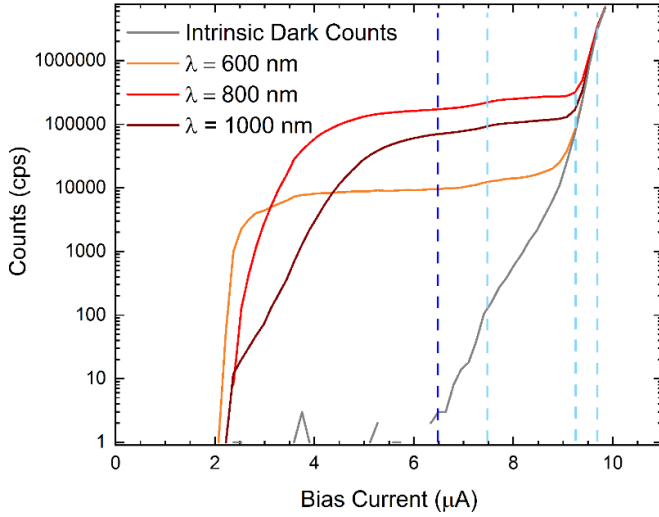


Figure 5. Counts versus bias for the $30 \times 30 \mu\text{m}$ active-area SNSPD studied in the main text. Non-normalized bright counts were measured with a filtered white light source and dark counts were measured with the system capped. The bias currents used for bright count (dashed dark blue) and dark count (dashed light blue) histogram and waveform measurements are indicated.

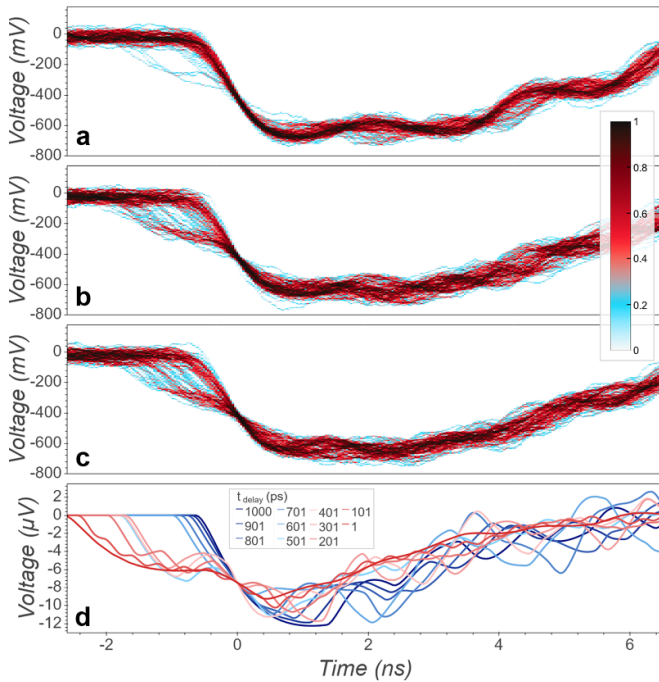


Figure 6. 100 waveforms of the bright count data collected in digital persistence mode at $\mu = 0.01$ and for spot sizes of (a) $7 \mu\text{m}$ and (b) $23 \mu\text{m}$. (c) 100 waveforms of dark count data for the typical operating bias current of $6.50 \mu\text{A}$. Waveforms are inverted by the cryoamplifier. (d) Simulated waveforms for photons incident at 11 positions on the nanowire defined by the microwave propagation time along the nanowire (shorter propagation times correspond to positions closer to the device readout).

again has a large $10 \mu\text{H}$ inductance. The third device is a small $5 \times 5 \mu\text{m}$ active-area telecom wavelength SNSPD with a 60 nm width, 50% fill fraction, small $0.6 \mu\text{H}$ inductance, and two-channel readout geometry. The second large-active-area

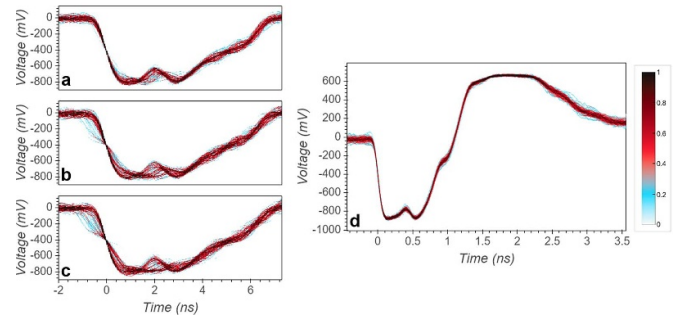


Figure 7. Waveforms from a $30 \times 30 \mu\text{m}$ active-area visible wavelength SNSPD with a 115 nm nanowire width and from a $5 \times 5 \mu\text{m}$ active-area telecom wavelength SNSPD with a 60 nm nanowire width. For the large-area device three cases are collected with 100 waveforms at a bias of $10.02 \mu\text{A}$ just before the start of the device plateau: bright counts at spot sizes of (a) $7 \mu\text{m}$ and (b) $23 \mu\text{m}$ and for (c) dark counts. For the small-area device 98 dark count waveforms are collected at a bias of $21.02 \mu\text{A}$ at the end of the device plateau (d). All waveforms are inverted due to the cryoamplification.

device thus has a shorter meander line length of 3.93 mm , and the waveforms are collected for both large spot size illumination ($23 \mu\text{m}$) and for small spot size illumination ($7 \mu\text{m}$), as shown in figures 7(a) and (b). The waveforms were collected at a bias current of $10.02 \mu\text{A}$, which is just below the plateau for this device with 2–4 dark counts per second. The bright counts are collected with the same 400 nm excitation source as in the main text at $\mu = 0.01$ photons per pulse and the resulting waveforms match the trends for the 4.79 mm length device studied in the main text. In particular, we note oscillations in the rising edge of the waveform that are more likely to appear when a larger area of the device is illuminated, demonstrating that position sensitivity is also evident in a second large active-area device. We further note that the frequency of these ripples is faster in these shorter 3.93 mm devices (with sinusoids at 0.4 and 0.7 GHz), indicating that the pulse echo analysis is consistent with this second device. Finally, the dark count waveforms shown in figure 7(c) are most similar to the large spot size waveforms, providing additional evidence that dark counts do originate from positions across the entire device.

To determine if a small-active-area device shows any of the characteristics of the two large area devices, dark count waveforms were collected from the third device which has a total meander line length of $208 \mu\text{m}$. The waveforms, collected at a bias current of $21.02 \mu\text{A}$ where there are around 40 dark counts per second at the end of the plateau, are shown in figure 7(d), and there is distinctly no ripple in the rising edge of the waveforms and no noticeable variation between the waveforms. However, the characteristic oscillation frequency of the waveforms is much faster than the large-active area devices, with a frequency of approximately 2.2 GHz , consistent with pulse echos occurring in the much shorter length of the device meander line combined with the smaller kinetic inductance of the device. Overall, this indicates that smaller active-area devices, with a much shorter meander line length and smaller

kinetic inductance, still have pulse echos of the propagating microwave signal. However the length of the meander line does not appear to be long enough for this to create a position-dependent variation to the pulse echos and thus to the dark count readout waveforms.

ORCID iDs

Claire E Marvinney  <https://orcid.org/0000-0002-0289-8059>

Brian E Lerner  <https://orcid.org/0000-0002-6406-9790>

Alexander A Poretzky  <https://orcid.org/0000-0002-9996-4429>

Benjamin J Lawrie  <https://orcid.org/0000-0003-1431-066X>

References

- [1] Hadfield R H, Habif J L, Schlafer J, Schwall R E and Nam S W 2006 *Appl. Phys. Lett.* **89** 241129
- [2] Takemoto K, Nambu Y, Miyazawa T, Sakuma Y, Yamamoto T, Yoroze S and Arakawa Y 2015 *Sci. Rep.* **5** 14383
- [3] Zhang Z, Chen C, Zhuang Q, Wong F N and Shapiro J H 2018 *Quantum Sci. Technol.* **3** 025007
- [4] Sun Q-C *et al* 2016 *Nat. Photon.* **10** 671
- [5] Graffitti F, Pickston A, Barrow P, Proietti M, Kundys D, Rosset D, Ringbauer M and Fedrizzi A 2020 *Phys. Rev. Lett.* **124** 010503
- [6] Hochberg Y, Charaev I, Nam S-W, Verma V, Colangelo M and Berggren K K 2019 *Phys. Rev. Lett.* **123** 151802
- [7] Ahmed Z *et al* 2018 (arXiv:1803.11306)
- [8] Natarajan C M, Tanner M G and Hadfield R H 2012 *Supercond. Sci. Technol.* **25** 063001
- [9] Eisaman M D, Fan J, Migdall A and Polyakov S V 2011 *Rev. Sci. Instrum.* **82** 071101
- [10] Zhao Q Y, Zhu D, Calandri N, Dane A E, McCaughan A N, Bellei F, Wang H Z, Santavica D F and Berggren K K 2017 *Nat. Photon.* **11** 247
- [11] Cahall C, Nicolich K L, Islam N T, Lafyatis G P, Miller A J, Gauthier D J and Kim J 2017 *Optica* **4** 1534
- [12] Nicolich K L, Cahall C, Islam N T, Lafyatis G P, Kim J, Miller A J and Gauthier D J 2019 *Phys. Rev. Appl.* **12** 034020
- [13] Zhu D, Colangelo M, Chen C, Korzh B A, Wong F N, Shaw M D and Berggren K K 2020 *Nano Lett.* **20** 3858
- [14] Li H, Zhang L, You L, Yang X, Zhang W, Liu X, Chen S, Wang Z and Xie X 2015 *Opt. Express* **23** 17301
- [15] Wang H *et al* 2019 *Appl. Opt.* **58** 8148
- [16] Allmaras J P, Wollman E E, Beyer A D, Briggs R M, Korzh B A, Bumble B and Shaw M D 2020 *Nano Lett.* **20** 2163
- [17] Zhang C *et al* 2019 *AIP Adv.* **9** 075214
- [18] Lv C *et al* 2017 *Supercond. Sci. Technol.* **30** 115018
- [19] Clem J R and Kogan V 2012 *Phys. Rev. B* **86** 174521
- [20] Zhao Q-Y, Santavica D F, Zhu D, Noble B and Berggren K K 2018 *Appl. Phys. Lett.* **113** 082601
- [21] Berggren K K, Zhao Q-Y, Abebe N, Chen M, Ravindran P, McCaughan A and Bardin J C 2018 *Supercond. Sci. Technol.* **31** 055010
- [22] Hadfield R, Miller A J, Nam S W, Kautz R L and Schwall R E 2005 *Appl. Phys. Lett.* **87** 203505
- [23] Kerman A J, Yang J K, Molnar R J, Dauler E A and Berggren K K 2009 *Phys. Rev. B* **79** 100509
- [24] Liu D, You L, Chen S, Yang X, Wang Z, Wang Y, Xie X and Jiang M 2013 *IEEE Trans. Appl. Supercond.* **23** 2200804
- [25] Engelhardt M Ltspice xvii(x64) (available at: <https://www.analog.com/en/design-center/design-tools-and-calculators/ltspice-simulator.html>) (2020-04-16)
- [26] Santavica D F, Adams J K, Grant L E, McCaughan A N and Berggren K K 2016 *J. Appl. Phys.* **119** 234302